HSP90-Specific nIR Probe Identifies Aggressive Prostate Cancers: Translation from Preclinical Models to a Human Phase I Study

Takuya Osada[1], Erika J. Crosby[1], Kensuke Kaneko[1], Joshua C. Snyder[1], Joshua D. Ginzel[1], Chaitanya R. Acharya[1], Xiao-Yi Yang[1], Thomas J. Polascik[1], Ivan Spasojevic[2,3], Rendon C. Nelson[4], Amy Hobeika[1], Zachary C. Hartman[1], Leonard M. Neckers[5], Andre Rogatko[6], Philip F. Hughes[7], Jiaoti Huang[8], Michael A. Morse[1,2], Timothy Haystead[7], and H. Kim Lyerly[1]

ABSTRACT

A noninvasive test to discriminate indolent prostate cancers from lethal ones would focus treatment where necessary while reducing overtreatment. We exploited the known activity of heat shock protein 90 (Hsp90) as a chaperone critical for the function of numerous oncogenic drivers, including the androgen receptor and its variants, to detect aggressive prostate cancer. We linked a near-infrared fluorescing molecule to an HSP90 binding drug and demonstrated that this probe (designated HS196) was highly sensitive and specific for detecting implanted prostate cancer cell lines with greater uptake by more aggressive subtypes. In a phase I human study, systemically administered HS196 could be detected in malignant nodules within prostatectomy specimens. Single-cell RNA sequencing identified uptake of HS196 by malignant prostate epithelium from the peripheral zone ($AMACR^+ERG^+EPCAM^+$ cells), including SYP^+ neuroendocrine cells that are associated with therapeutic resistance and metastatic progression. A theranostic version of this molecule is under clinical testing.

Introduction

Screening for prostate cancer currently relies on serologic testing of PSA levels; however, many prostate cancers detected by rising PSA levels behave indolently (1–3), and, thus, many patients undergo unnecessary biopsies and therapy. This highlights the need for a noninvasive modality to focus attention on early malignancies with more aggressive biological potential.

Hallmarks of aggressive biological behavior such as rapid local invasion and distant spread require high levels of molecules that drive cellular growth and differentiation (4–6), many of which rely on the chaperone heat shock protein 90 (Hsp90) for their proper conformation and function (7–9). Indeed, Hsp90 expression and behavior is often altered in poor-prognosis malignancies (10–14).

Therefore, *in vivo* detection of Hsp90 could serve as a noninvasive method for identifying clinically aggressive malignancies. We demonstrated in preclinical models of breast cancer (15) that HSP90 could be used as an imaging target to identify breast cancers with aggressive phenotypes (16, 17).

In vivo molecular imaging frequently depends on radioactive probes that can be detected by SPECT or PET imagers. Hsp90-targeted PET imaging using [124]I-tethered Hsp90 inhibitor (PU-H71) was shown to detect various cancer types, including prostate and breast cancers, demonstrating tumor-selective accumulation and long retention of the radiotracer (18). To avoid the complexities of nuclear medicine imaging, we linked a near-infrared (nIR) probe to an analogue of the Hsp90 ATP-binding domain inhibitor SNX-5422 (15, 19). This Hsp90-targeting nIR probe, while capable of imaging all molecular subtypes of murine and human BC, was more effectively taken up by aggressive and highly metastatic clones (15). For the current work, we developed a new Hsp90-targeting probe (HS196) linked to an nIR molecule that fluoresces at a longer wavelength, allowing imaging of deeper structures. We tested this probe in preclinical prostate models, developed a clinical-grade reagent, and performed a phase I dose escalation study to demonstrate safety and uptake in early prostate cancers. We found that this novel probe could discriminate indolent disease from aggressive—potentially reaching an unmet milestone in the diagnosis of life-threatening forms of prostate cancer.

Materials and Methods

Reagents

We have previously generated a series of Hsp90 inhibitors tethered to fluorophores to detect Hsp90 *in vivo* (20). One of these molecules, HS131, consists of an Hsp90 inhibitor tethered to a cyanine dye, which has an excitation wavelength of 640 nm and an emission wavelength of 680 nm. For the potential clinical application as an *in vivo* imaging reagent, we aimed to achieve deeper tissue penetration and better visualization of malignant lesions, and thus developed a similar more

[1]Department of Surgery, Duke University Medical Center, Durham, North Carolina. [2]Department of Medicine, Duke University Medical Center, Durham, North Carolina. [3]Pharmacokinetics/Pharmacodynamics Core Laboratory of Duke Cancer Institute, Durham, North Carolina. [4]Department of Radiology, Duke University Medical Center, Durham, North Carolina. [5]Urologic Oncology Branch, NCI, Rockville, Maryland. [6]Biostatistics and Bioinformatics Research Center, Samuel Oschin Comprehensive Cancer Institute, Cedars-Sinai Medical Center, Los Angeles, California. [7]Department of Pharmacology and Cancer Biology, Duke University, Durham, North Carolina. [8]Department of Pathology, Duke University Medical Center, Durham, North Carolina.

Corresponding Author: H. Kim Lyerly, Surgery, Duke University Medical Center, 203 Research Drive, Suite 433, Durham, NC, 27710. Phone: 919-681-8350; E-mail: kim.lyerly@duke.edu

soluble molecule, denoted HS196, with peak absorption at 790 nm and peak emission at 800 nm. To evaluate nonspecific dye uptake, HS199, an nIR dye lacking an Hsp90 binding moiety, was developed as a control molecule. The synthesis methods for HS196 and HS199 were similar to those reported previously for HS131 (19). The detailed HS196 synthesis method is shown in Supplementary Methods. Clinical-grade HS196 for use in the phase I clinical trial was produced by Albany Molecular Research Inc. (AMRI) and filled and finished by Berkshire Sterile Manufacturing. Toxicology studies were performed by Charles River Laboratories.

Cancer cell lines and culture

Four human prostate cancer cell lines, PC-3 (CRL-1435), DU145 (HTB-81), 22Rv1 (CRL-2505). and LNCaP (CRL-1740), with different aggressiveness (21–24) were purchased from ATCC. The ATCC uses short tandem repeat profiling for testing and authentication of cell lines. Cells were thawed, subcultured, and expanded per ATCC recommendations, and stored in liquid nitrogen as cryopreserved aliquots within five passages of their purchase from ATCC. For *in vitro* and *in vivo* experiments, PC-3 and DU145 cells were thawed and cultured in Dulbecco's modified Eagle's medium supplemented with 10% FBS, 100 U/mL of penicillin, and 0.1 mg/mL of streptomycin at 37°C in a humidified 5% CO_2 atmosphere. 22Rv1 and LNCaP cells were cultured in RPMI-1640 medium supplemented with 10% FBS, penicillin/streptomycin, and L-glutamine. Cell lines were used in experiments within 3 passages after thawing of frozen aliquots, and were tested for *Mycoplasma* every 3 to 6 months as a part of routine monitoring in the laboratory.

Animals

SCID-beige mice were originally purchased from Charles River and maintained in the Duke University Cancer Center Isolation Facility in accordance with the Institutional Animal Care and Use Committee guidelines. All experiments and mouse euthanasia were conducted according to IACUC-approved protocols (A294-11-11, A254-14–10, A216-17-09, and A164-20-08).

For the imaging of human prostate cancer xenografts, including PC-3, DU145, 22Rv1, and LNCaP, $1 \times 10E6$ cells were resuspended in 50% Matrigel/50% saline, and subcutaneously injected to the flank of SCID-beige mice. Once the tumor sizes reached 10 mm in diameter, mice were imaged.

Fluorescent imaging and measurement

For the imaging of tumors in mice, HS196 or HS199 (0.1–100 nmol) was dissolved in DMSO (20 μL per injection) and administered via tail vein. Mouse whole body images were taken over time using the LI-COR Pearl Trilogy imaging system (LI-COR Biosciences), whereas mice were anesthetized with 2% isoflurane. The 800-nm channel of the system was used for the detection of fluorescence signals of HS196 and HS199, and the fluorescence signals were analyzed using ImageStudio software (version 5.0.21, LI-COR). Selected regions of interest covering the tumor area were analyzed for fluorescence intensity and fluorescence intensity per area. For more accurate analysis of HS196/HS199 accumulation to the tumors, *ex vivo* imaging of tumors was performed using the LI-COR Pearl Imager after euthanasia of the mice.

Flow cytometry

Tumor cells cultured *in vitro* were harvested with 0.05% trypsin/EDTA and washed with PBS three times. Cells were resuspended in media and HS196 or HS199 were added to a final concentration of 10 μmol/L. Cells were incubated in CO_2 incubator at 37°C for 30 minutes, then washed with PBS three times, stained with viability dye (Thermo Fisher Scientific) and acquired on an LSRII (red laser, APC-Cy7 channel, filter 780/60; BD Biosciences). Data analysis was performed using FlowJo software (FlowJo LLC).

For the analysis of tumor cells from *in vivo* tumors, tumors were minced with a razor blade and digested for 1.5 hours at 37°C with triple enzyme buffer, which includes collagenase III (1 mg/mL; Worthington), hyaluronidase (0.1 mg/mL, Sigma), and deoxyribonuclease (20 U/mL, Sigma). Tumor digests were passed through a 40-μm cell strainer, washed with PBS three times, and acquired on an LSRII flow cytometry machine (BD Biosciences).

Fluorescence microscopy analysis

PC-3 cells were incubated on glass-bottomed dishes (MatTek) overnight, then incubated with HS196 or HS199 (10 μmol/L) in the culture medium for 1 hour at 37°C. Cells were then washed with PBS three times and fixed with 10% neutral buffered formalin. After formalin fixation, cells were stained with Alexa Fluor 488–conjugated wheat germ agglutinin (WGA) membrane staining dye (5 μg/mL; Thermo Fisher) for 30 minutes at room temperature. Following WGA staining, imaging was performed on a Zeiss LSM 880 microscope with a 40× objective (Carl Zeiss AG). Because of its broad excitation spectrum (600–820 nm), the HS196 probe was detectable by excitation using a 633-nm laser. The Alexa Fluor 488–conjugated WGA was excited using a 488-nm laser.

Human tumor tissue was frozen in OCT compound after harvest and cut into 5-μm-thick sections. Serial sections were used for correlative H&E pathology and RNA FISH. RNAscope Multiplex Fluorescent kit (cat no: 323100, Advanced Cell Diagnostics) was used to detect target genes (*AMACR*-RNAscope Probe-Hs-AMACR-O1-C2, cat. #506501-C2; Advanced Cell Diagnostics) in frozen sections. Frozen tissue sections were prepared and pretreated prior to probe hybridization and signal development following the Multiplex Fluorescent kit user manual. Tiled images were acquired for each channel on a Zeiss LSM 880 microscope using a 40× objective (Carl Zeiss Microscopy LLC). HS196 probe was excited using a 633-nm laser, and the RNA FISH probe was excited using a 488-nm laser.

Pharmacokinetic (PK) analysis

Preclinical mouse (tumor-bearing), rat (GLP toxicokinetic; male and female), and clinical (phase I) PK were studied after intravenous injection of HS196 in a saline (0.9% sodium chloride) formulation followed by collection of blood at appropriate time points into anticoagulant (K_2EDTA)-containing tubes followed by centrifugation to separate plasma. Plasma samples were stored at −80°C until the analysis. For the mouse PK study, tumor and several organs/tissues were collected at the same time points as blood and stored at −80°C along with plasma samples. The HS196 was analyzed by LC/MS/MS (Duke PK/PD Core). In brief, extraction from plasma was accomplished by solid-phase extraction (Waters Oasis WAX, 10 mg) and from tissue homogenate (tissue cryo-pulverized and homogenized with two parts water) by liquid–liquid extraction with two parts methanol. After separation on reversed phase LC column (Zorbax Eclipse 4.6 × 50 mm, 1.8 μm, Agilent) by 10 mmol/L ammonium hydroxide/methanol gradient (45%–75% methanol, 4 minutes), detection was performed by tandem-mass instruments API 6500+, API 5500, or API 4000, AB SCIEX LLC) under the following MS/MS transitions: 773.0/336.15 (HS196) and 787.0/336.15 (HS199, internal standard, closely related analogue). Lower limit of quantification was 0.81 ng/mL.

PK modeling and calculations were performed by compartmental and noncompartmental methods within WinNonlin software (Pharsight).

Phase I clinical trial

The clinical phase I clinical trial was conducted in accordance with International Conference on Harmonization Guidelines for Good Clinical Practice and the Code of Federal Regulations and guided by the ethical principles of the Belmont Report, under an FDA-approved Investigational New Drug Exemption and registered at ClinicalTrials.gov (NCT03333031). Participants were recruited from medical, surgical, and urologic oncology clinics at Duke University Medical Center, Durham, NC, and provided written informed consent under a protocol approved by the Duke University Medical Center Institutional Review Board. The protocol was originally written to enroll patients, age ≥18 years, with a diagnosis of (or suspected) solid malignancy, stages I–IV, for which surgery or biopsy was planned; however, early in the study, based on our preliminary data and interest of clinical collaborators, a decision was made to focus on prostate cancer patients who would be undergoing radical prostatectomies. All were required to have ECOG Performance Score 0 or 1, estimated life expectancy > 3 months, and adequate hematologic, renal, and hepatic function. A safety study with the estimation of the maximum tolerated dose was performed by a dose escalation strategy referred to as EWOC (Escalation With Overdose Control). Toxicity was assessed using CTCAE version 4.0 toxicity criteria. The doses selected for each patient in the trial (in mg) was planned to be one of the following 0.5, 1, 2, 4, 6, 7, 8, 9, or 10 mg. No dose was skipped during a dose escalation. For this publication, the 7-mg dose was the last dose utilized. HS196 was administered as a single 5-mL slow intravenous push (1 mL per minute) over a maximum of 15 minutes followed by a saline flush. Administration of HS196 was required to occur within 36 hours prior to the scheduled start time for surgery to resect the malignancy. Tissue from the surgery as available was tested in the LI-COR Odyssey CLx for *ex vivo* imaging of tumors. Fluorescence images of gross specimens were generated using a hand-held Fluobeam device (Fluoptics). Slices of tumor were visualized with a NIR microscope. Standard-of-care MRI scans of the pelvis were obtained for review.

Single-cell RNA-seq of prostate cancer tissue

Following visualization with NIR microscopy, sections of tumor that were positive for HS196 signal were dissected and enzymatically digested. Red blood cells were lysed with Red Blood Cell Lysis buffer (Sigma R7757) for 5 minutes, and stained with LIVE/DEAD Fixable Green Dead Cell Stain (Thermo Fisher). Live, single cells from the tumor suspension were sorted by flow cytometry into HS196$^+$ (top 2% of cells) and HS196$^-$ (bottom 25% of cells) portions. 10× libraries were created using Chromium Single-Cell 5' Library Construction Kits (v1.1; 10X Genomics) following the manufacturer's protocol. A targeted cell recovery of 7,000 cells was used for each tumor sample. Gene-expression libraries were created for each sample. Generated cDNA and final GEX libraries were quality checked using an Agilent Bioanalyzer 2100 at Duke Microbiome Core Facility and submitted to MedGenome Inc. for sequencing on a NovaSeq S4 instrument. All RNA-seq data have been deposited in the NCBI GEO and are available under the accession number GSE164865.

Single-cell RNA-seq analysis

Fastq files from 10X library sequencing were processed using Partek Genomics Suite software (version 9.0.20; Partek Inc). Sequences were aligned to the hg19 reference genome (STAR aligner 2.7.3a, RRID: SCR_015899), and UMI counts were deduplicated and filtered to include only barcodes that corresponded to a cell. Transcripts were quantified and single-cell counts were filtered to include cells with total reads between 500 and 25,000, expressed genes 15 and 5,000, and a maximum of 25% mitochondrial reads. Counts were normalized to counts per million and $\log_2$ transformed. Clusters, identified using shared nearest neighbor (SNN)-based clustering on the basis of the top 100 principal components, were visualized using UMAP plots using the first 13 principal components, a minimum distance of 0.4, 30 neighbors (25). Differentially expressed genes were identified using the GSA algorithm in Partek Flow. Visualizations were created using Partek Flow (Partek Inc) and GraphPad Prism (GraphPad Software). Aligned sequences were extracted using CellRanger (10X Genomics). Clustering, cell type identification, and differential gene-expression analysis of single-cell data were done with treatment groups deidentified for blinding.

Statistical analysis

The differences in the fluorescence intensities in imaging studies were analyzed by the Student *t* test or one-way ANOVA test with adjustment for Tukey multiple comparison using GraphPad Prism software.

Results

Uptake and retention of HS196 in prostate cancers is concentration dependent

We previously reported HSP90-specific uptake of an HSP90-nIR conjugate (HS131) in a variety of breast cancers. For the current study, in order to allow greater penetration of the nIR energy for imaging deeper tumor, we produced a water-soluble imaging probe (called HS196) by linking the Hsp90 inhibitor to a different nIR dye (**Fig. 1A**) with peak absorption at 790 nm and peak emission at 800 nm (**Fig. 1B**). As a control, we also generated HS199, which consists of an inactive form of Hsp90 inhibitor unable to bind to Hsp90, linked to the same soluble nIR dye (**Fig. 1A**). Because our previous studies with the HS131 were performed in breast cancer models, for the present study, we determined the dose that resulted in the optimal tumor to background fluorescence ratio for HS196 using an implanted breast cancer model. Following intravenous administration of HS196, the absolute fluorescence of HS196 from tumor and background increased as the dose increased (Supplementary Fig. S1A and S1B), but the dose of HS196 that provided the optimal tumor to background fluorescence ratio was in the range of 10 to 25 nmol (Supplementary Fig. S1C), resulting in high and prolonged tumor uptake (Supplementary Fig. S1D) but minimal normal tissue uptake except for liver and kidney (Supplementary Fig. S1E).

Because we were interested in studying the HS196 in prostate cancer, we then assessed the uptake of HS196 by prostate cancer cell lines. We could detect the HS196 fluorescence of *ex vivo* labeled PC-3 human prostate cancer cells by confocal microscopy (**Fig. 1C**), flow cytometry (**Fig. 1D**), and *in vivo* in implanted PC-3 cells by the LI-COR Pearl (800 nm channel; **Fig. 1E**).

Uptake of HS196 by tumor is dependent on HSP90 binding

To demonstrate that HS196 uptake was dependent on its binding to Hsp90, we compared the tumor uptake of HS196 and HS199 (which is unable to bind to Hsp90) in PC-3 human prostate cancers *in vivo* (**Fig. 2**). Tumor fluorescence for HS196 exceeded that for HS199 at all time points after injection (**Fig. 2A** and **B**), suggesting prolonged tumor retention of HS196 is dependent on binding to Hsp90. We
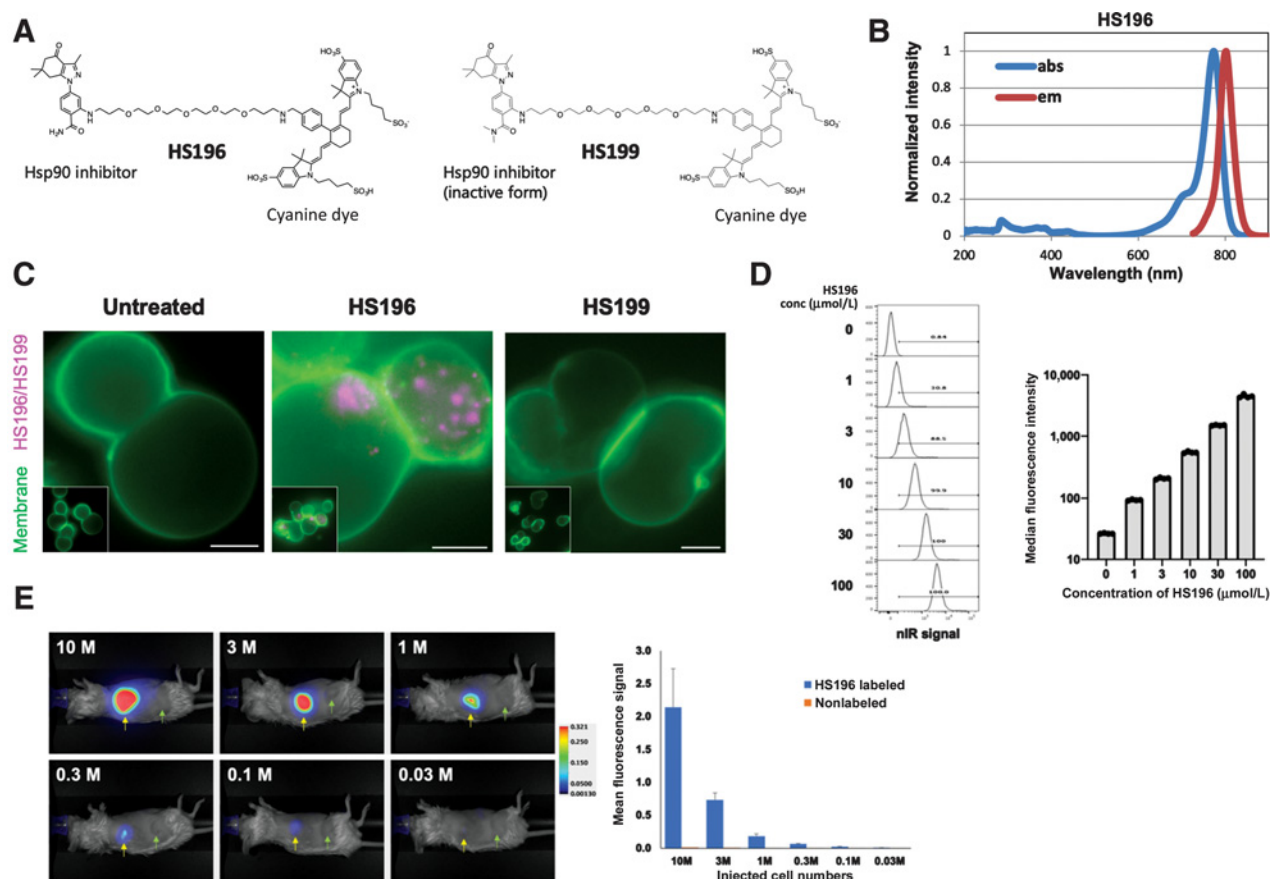
Osada et al.

Figure 1.

Structure and characteristics of nIR dye–tethered Hsp90 inhibitor HS196. **A,** Chemical structures of HS196 and HS199. **B,** Absorption and emission peak of HS196. **C,** Fluorescence microscope analysis of HS196 uptake by PC-3 prostate cancer cells *in vitro*. PC-3 cells cultured in glass-bottomed dish were incubated with HS196 or HS199 (10 μmol/L in medium) for 1 hour, washed with the medium, and then fixed with 5% formalin for 30 minutes. WGA Alexa Fluor 488 membrane dye was applied to the dishes to stain cell membrane. Images were acquired using Zeiss LCM880 Confocal Laser Microscope. Membrane: green, nIR: red. Scale bar: 10 μm. **D,** Detection of the nIR signal of HS196-labeled cancer cells by flow cytometry. PC-3 cells were labeled with HS196 at 0, 1, 3, 10, 30, or 100 μmol/L for 30 minutes, and then washed with PBS three times. Cells were acquired by LSRII flow cytometry machine. Percentage of nIR-positive cells is shown in each histogram and median fluorescence intensity in the graph (*n* = 4 for each concentration). Red laser (633 nm) and 780/60 detector were used. **E,** nIR signal detection of HS196-labeled PC-3 cells *in vivo*. PC-3 cells were labeled with HS196 (10 μmol/L) for 30 minutes, and then washed with PBS three times. Different number (10M, 3M, 1M, 0.3M, 0.1M, and 0.03M) of HS196-labeled PC-3 cells or nonlabeled PC-3 cells was resuspended in 100 μL saline and subcutaneously injected to the flank of SCID-beige mice (yellow arrow: HS196-labeled PC-3, green arrow: nonlabeled PC-3). nIR signals were assessed for 3 injection sites of HS196-labeled PC-3 cells for each cell numbers by LI-COR Pearl (800-nm channel). Mean fluorescence signals are shown on the right. Error bar: SD.

confirmed that the uptake of HS196 was tumor-specific by analyzing fluorescence of resected bulk tumor *ex vivo* (**Fig. 2C**), localization of HS196 to prostate cancer cells (**Fig. 2D**) by confocal microscopy, and by flow-cytometric analysis of single cells from tumor digests (**Fig. 2E**).

Uptake and retention of HS196 is enhanced in prostate cancer cells with more aggressive characteristics

We previously demonstrated Hsp90-specific uptake of HS131, our prototype Hsp90-targetted probe, into more aggressive breast cancers in our prior work (15). We therefore wished to determine whether similar observations would be made with other tumor types where more accurate diagnosis remains a challenge such as human prostate cancer. Using human prostate cancer cell lines, we demonstrated greater HS196 fluorescence intensity within the aggressive androgen receptor (AR)-negative, androgen-irresponsive prostate cancer cell line PC3 and moderately aggressive AR-negative, andro-

gen-irresponsive cell line DU145, and least in the indolent androgen-responsive cell line LNCaP (**Fig. 2F**). We also tested the HS196 uptake by the 22Rv1 cell line, which expresses constitutively active splice variants of AR (26, 27), grows in an androgen-independent manner, and possesses features of clinically aggressive, therapy-resistant disease. When the two AR-positive prostate cancer cell lines, 22Rv1 and LNCaP, were compared, greater HS196 fluorescence intensity was demonstrated for the 22Rv1 tumors compared with the LNCaP tumors *in vivo*. These data indicate that HS196 selectively identifies aggressively behaving prostate cancers.

Preclinical pharmacokinetics

In tumor-bearing mice, the PK profile of plasma, tumor, and organs/tissue was investigated over 7 days. Detailed parameters of plasma PK analysis are shown in Supplementary Table S1. The plasma concentration/time profile reveals multiple processes with
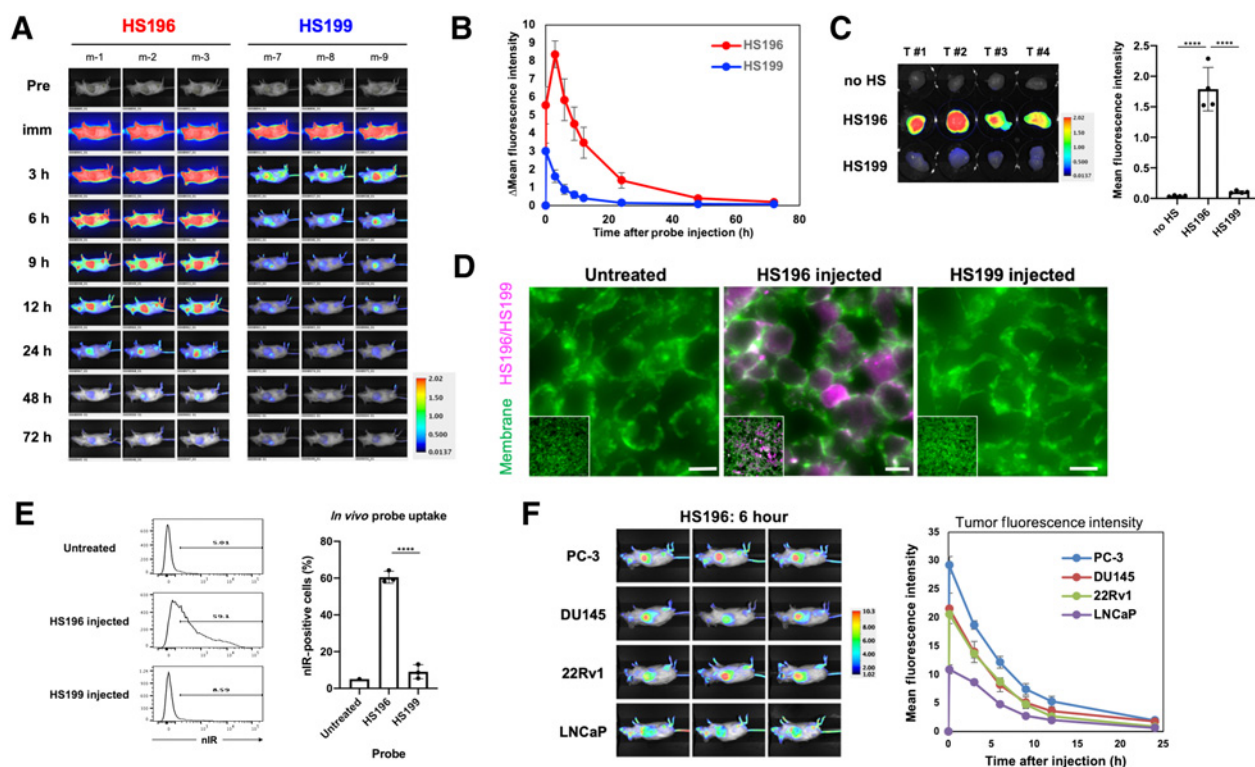
Figure 2.
Imaging of human prostate cancer xenograft PC-3 in SCID-mice with Hsp90-targeted Probe HS196. **A,** SCID-beige male mice were subcutaneously implanted with PC-3 cells (1 × 10E6 cells/mouse) to the flank. When tumor size reached 8–10 mm in diameter, mice were administered HS196 or HS199 (10 nmol/inj) via tail-vein injection. Temporal dynamics of nIR signal from PC-3 tumor was analyzed using LI-COR Pearl Imager (800 nm channel). Six mice were tested for each probe. Representative 3 mice for each probe are shown. **B,** MFI of the background area was subtracted from MFI of tumor area and plotted for each group ($N = 6$ mice for each group). Error bar: SE. **C,** *Ex vivo* images of PC-3 tumors. Tumors were excised from mice 24 hours after the administration of HS196/HS199 (10 nmol/mouse) or no HS injection (untreated control). $N = 4$ tumors for each group. Error bar: SD. One-way ANOVA test was performed with Tukey multiple comparison adjustment. ****, $P < 0.0001$. **D,** Confocal microscope images of PC-3 tumors excised from mice 6 hours after the administration of HS196 or HS199 (10 nmol/mouse) via tail-vein injection. Membrane: green, nIR: red. Scale bar: 10 μm. **E,** Flow cytometry of single-cell digests. Six hours after the administration of HS196 or HS199 (10 nmol/mouse, $n = 3$ mice for each), mice were euthanized and harvested tumors were minced and digested with collagenase III/hyaluronidase/DNase for 1 hour at 37°C, and washed with PBS. Isolated cells were labeled with live/dead dye, followed by FITC-conjugated anti-HLA class 1 mAb. Cells were acquired using LSRII flow cytometer, and nIR signals in alive HLA-positive PC-3 cells were analyzed using red laser, APC-Cy7 channel with 780/60 filter. Representative histograms for each probe are shown, and percentages of nIR-positive cells among PC-3 tumor cells are shown in the right graph. Untreated tumor sample (tumor from a mouse without probe injection) is shown as a reference. Error bar: SD. Student *t* test was performed between HS196 and HS199 groups. ****, $P < 0.0001$. **F,** Comparison of *in vivo* HS196 uptake by 4 different prostate cancer lines with different metastatic capacities. One million cells of PC-3, DU145, 22Rv1, or LNCaP cell line were resuspended in 50% Matrigel/ 50% saline and subcutaneously implanted to the flank of male SCID-beige mice (PC-3: 6 mice; DU145: 8 mice; 22Rv1: 5 mice, LNCaP: 3 mice). When tumor size reached approximately 10 mm in diameter, HS196 (10 nmol/mouse) were administered via tail-vein injection. nIR signals were analyzed as described above until 24 hours. Representative whole body images of 3 mice for each prostate cancer xenograft at 6 hour time point are shown. Mean fluorescence intensities of tumor areas are plotted for each prostate tumor line. Error bar: SE.

two main exponential decays (presumably distribution to tissues and elimination from the central compartment) responsible for 97% of the extrapolated initial concentration of HS196 within the first 8 hours (**Fig. 3**). Importantly, we observed higher concentrations and longer retention of HS196 in tumor tissue compared with other major organs (e.g., brain, lung, liver, and kidney) and tissues (e.g., muscle, fat, and skin). HS196 concentrations begin exceeding other tissue concentrations within the first few hours and all tissues by 24 hours. These data support the feasibility of imaging with HS196 based on its tumor selectivity. Clearance was low (0.1 L/h/kg), i.e., 1.2% of total plasma cardiac output (~8.6 L/h/kg in adult mouse; using average mouse hematocrit 41%; ref. 28). Volume of distribution at steady state ($V_{ss} = 0.265$ L/kg; average from noncompartmental and compartmental modeling;

Supplementary Table S1) was ~6-fold higher than total plasma volume (~0.046 L/kg in adult mouse; ref. 29), suggesting high distribution of HS196 to tissues, as proven by both fluorescence and LC/MS/MS measurements. Average mouse hematocrit (41%) was used for plasma volume calculations (30).

Phase I human study: patients, treatment, and plasma pharmacokinetics

Six patients were enrolled and received HS196 between October 11, 2018, and January 9, 2020. Demographics are reported in **Table 1**. Five had prostate cancer and one had a biliary malignancy. The doses received were 0.5, 1, 2, 4, 6, and 7 mg. One prostate cancer patient did not proceed to surgery due to medical issues unrelated to study drug administration. There were no adverse events referable to the HS196,
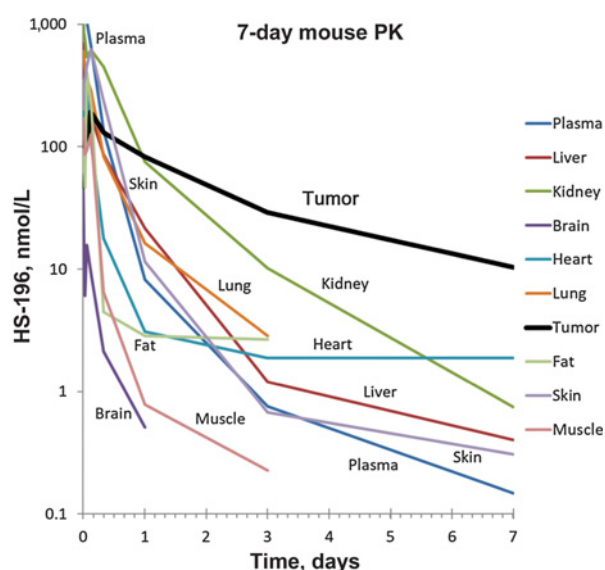
Figure 3.
Preclinical PK-PD analysis. 1 mg/kg of HS196 was intravenously injected to tumor-bearing SCID-beige mice. Blood and organs/tissues were collected from 3 mice for each time point (5 minutes, 15 minutes, 30 minutes, 1.5 hours, 3 hours, 8 hours , 24hours , 72 hours, and 168 hours). Plasma was isolated and stored at -80°C until the analysis. Organs/tissues were cryopulverized and homogenized and then stored at -80°C. Plasma and tissue homogenate were analyzed by LC/MS/MS for HS196 level.

Table 2. Adverse events.

Adverse event	Number of occurrences	Grade	Related to study drug
Dry eye	1	1	No
Scratchy throat	1	1	Yes
Eye swelling	1	1	No
Subconjunctival hemorrhage	1	1	No
Diplopia	1	1	No
Lymphedema	1	1	No

observed within first 4 hours. Average clearance was slightly lower than in mouse (0.07 L/h/kg), but considering a lower plasma cardiac output in human ($\sim$2.7 L/h/kg; ref. 28), relative clearance is higher than in mouse (2.6% vs. 1.2%, respectively). Volume of distribution, $V_{ss} = 0.47$ L/kg, was 12-fold higher when compared with total plasma volume in human ($\sim$0.04 L/kg; ref. 31), thus suggesting twice higher tissue distribution in human than in mouse. Average human hematocrit (44%) was used for plasma volume calculations (32).

Fluorescence imaging detected tumor avidity for HS196

When possible, resected gross tumor and sections were imaged *ex vivo* by the LI-COR Odyssey and Fluobeam Imagers. nIR images of representative cut specimens acquired by the LI-COR Imager are demonstrated in **Fig. 4**. For reference, preoperative T2-weighted and diffusion-weighted axial MR images of prostate tissues are shown on the left. The areas suspicious for prostate cancer are marked with white asterisks (center of tumors) and blue arrow heads (margin of tumors). The LI-COR Odyssey was able to detect HS196 in tissue sections at sites of gross tumor. To confirm that fluorescence represented tissue uptake of HS196, samples from sites of tissue (prostate or liver) with fluorescence were analyzed for concentration of HS196. The concentration of HS196 was greater in the tissues with fluorescence (Supplementary Fig. S2C) following HS196 administration than samples without fluorescence. Supplementary Fig. S3 shows nIR images of representative prostate tissue taken from the surface by Fluobeam Imager shortly after surgical resection.

except one patient reported dry eyes (**Table 2**). PK analyses demonstrated dose proportionality of the HS196 in peripheral blood (Supplementary Fig. S2A). Dose per kg of body weight provided the highest correlation with drug exposure as measured by AUC and C_{max} (Supplementary Fig. S2B), which should be considered in further stages of clinical studies. Detailed parameters of plasma PK analysis are shown in Supplementary Table S2. As in the preclinical testing, there were multiple processes with two main exponential decays

Table 1. Demographics of the patients.

Pt #	Age	Gender	Race	Ethnicity	Diagnosis	Stage	Gleason score	Preop therapy
1	57	Male	Caucasian	Not Hispanic or Latino	Prostate cancer	pT3aN0MxR0	3 + 4 = 7	No
2	56	Female	African American	Not Hispanic or Latino	Cholangiocarcinoma	No pathologic staging	N/A	No
3	70	Male	Caucasian	Not Hispanic or Latino	Prostate cancer	pT2N0MxR0	4 + 3 = 7	No
4	60	Male	African American	Not Hispanic or Latino	Prostate cancer	No pathologic staging (surgery not performed)	3 + 4 = 7	No
5	63	Male	Caucasian	Not Hispanic or Latino	Prostate cancer	pT2bN1MxR0	4 + 3 = 7	No
6	75	Male	Caucasian	Not Hispanic or Latino	Adenocarcinoma of unknown origin in periurethral tissue in patient with prior history of prostate cancer	Not staged	N/A	Brachy-therapy 17 years prior

Note: Demographics and tumor pathologic findings for each patient who received HS196 are listed. Because of the small amount of tumor at surgery, patient 2 did not have tumor tissue available for research studies, whereas normal liver tissue was available. Because the surgery for patient 4 was cancelled, and patient 6 had been treated previously with brachytherapy, surgical specimens from these 2 patients could not be provided for research studies.
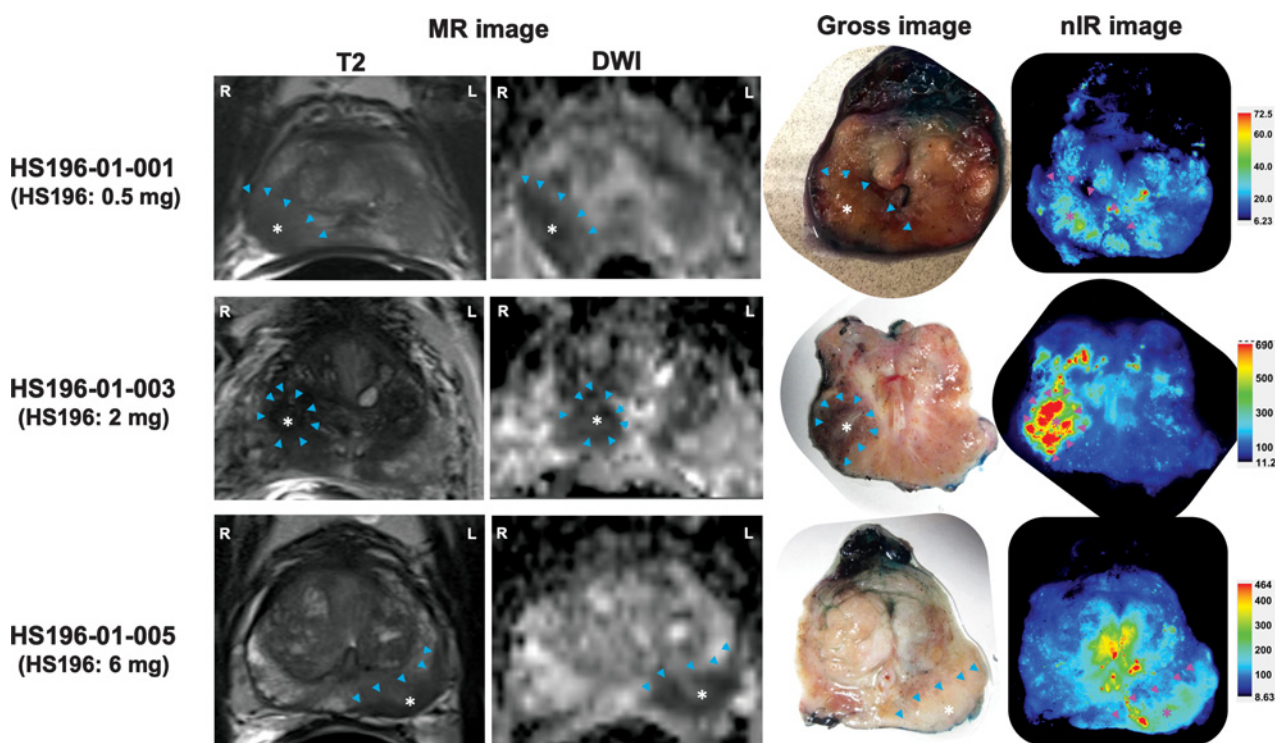
Figure 4.
Preoperative MR images and *ex vivo* imaging of resected prostate tissue. Preoperative axial MR images of the prostate (T2-weighted and diffusion-weighted), gross images, and nIR images of resected prostate tissues analyzed by LI-COR Odyssey imager are shown. In MR images, T2-weighted and diffusion-weighted hypointense prostate cancer lesions are marked with asterisks at the center and blue arrow heads at the margin (left 2 columns). Resected prostate tissues were cut, and gross images and nIR images of cut surfaces, analyzed using LI-COR Odyssey 800 nm channel, are shown (right 2 columns). Prostate cancer lesions are marked with asterisks and arrow heads.

Single-cell analysis detects uptake of HS196 by human prostate cancer cells

Patient prostatectomy samples were disaggregated and HS196 positive and negative cells were sorted for single-cell RNA-seq analysis (**Fig. 5**). Cells were clustered and cell types identified using canonical markers (Supplementary Fig. S4A). Multiple cell types were confirmed, including epithelial cells, stromal cells, and immune cells. To characterize the epithelial cells ($EPCAM^+$), this population was reclustered (**Fig. 5B**), and gene expression within these 6 new clusters was evaluated. Gene-expression analysis clearly distinguishes them into cells from the transition/central ($KRT13^+$, $SCGB1A1^+$) and peripheral zones ($KLK3^+$) of the prostate (**Fig. 5C**; ref. 33). Interestingly, most of the $EPCAM^+$ epithelial cells from the peripheral zone (clusters 1 and 4) were positively labeled with HS196 (98.5%), whereas the majority of HS196-negative epithelial cells were from the transition/central zone (clusters 2, 3, 5, and 6; 93.2%; **Fig. 5D**). Peripheral zone $HS196^+$ cells (clusters 1 and 4) showed high expression of known prostate tumor markers including *TMPRSS2*, *AMACR*, *ERG*, and *AR* (**Fig. 5E**). In addition, a population of peripheral zone $HS196^+$ cells also expressed *SYP* and *ENO2*, indicative of neuroendocrine cells, which have been linked to therapeutic resistance and progression of prostate cancer (Supplementary Fig. S4B; refs. 34, 35). Importantly, $AMACR^+$ $EPCAM^+$ prostate cancer cells were almost all HS196 positive (95.1%), showing the efficient labeling of *in vivo* cancer cells by HS196 (**Fig. 5F**). A small population of $AMACR^+$ HS196-positive cells were found in the transition zone, which may suggest multifocal occurrence of prostate cancer in the patient. $EPCAM^+$ cells expressing *SOX2* or *MYC*, key factors in inducing pluripotency in somatic cells and prostate cancer stem cells (36, 37), were also positively labeled with HS196, suggesting the possible therapeutic intervention against prostate cancer stem cells via Hsp90-targeting strategies (Supplementary Fig. S4C). Gene-expression analysis identified remaining populations as basal epithelium (cluster 2), a mixture of hillock ($KRT13^+$), and club cells ($SCGB1A1^+$; clusters 3 and 6, both with high *PSCA*) and a noncanonical cluster of prostate epithelium (cluster 5; Supplementary Fig. S5; ref. 33). These data suggest that HS196 taken up by malignant prostate epithelium in humans.

Confirmation of tumor cell uptake of HS196 by histology

Resected specimens were sectioned (5 μm), H&E stained, and whole-slide imaged. H&E pathology was coregistered with HS196 signal and an mRNA FISH image of the prostate cancer marker (*AMACR*) found in the peripheral prostate of HS196-positive epithelial cells (**Fig. 5G** and **H**). Pathologic assessment confirmed invasive prostate cancer (**Fig. 5H**) and when coregistered, confirmed the presence of HS196-positive and *AMACR*-expressing prostate cancer cells. These data demonstrate that HS196 is taken up in the malignant prostate epithelium including a subset of invasive *AMACR*-expressing prostate cells found in the peripheral prostate.

Discussion

The detection of localized cancers relies on physical exam and anatomic imaging that have modest sensitivity and specificity and
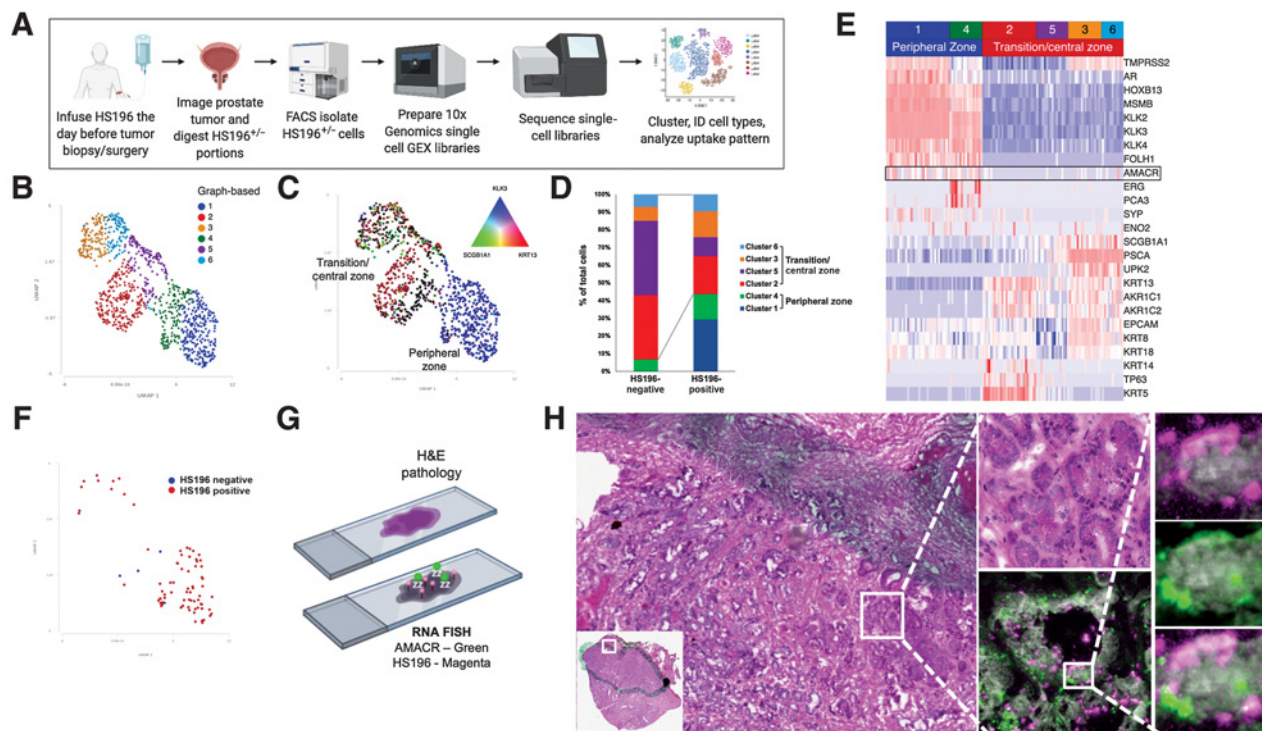
Figure 5.
Single-cell RNA-seq and confocal microscopy of prostate cancer specimen. **A,** Process of sample preparation for single-cell RNA-seq of prostate cancer specimen. HS196$^+$ and HS196$^-$ cell populations were isolated from enzymatically digested prostate specimen by flow-based sorting, and single-cell cDNA libraries were made and sequenced. **B,** EPCAM$^+$ epithelial cells were reclustered and shown in UMAP plot. Six different clusters were identified. **C,** Cells in peripheral zone and in transition/central zone were identified based on gene expression of KLK3, KRT3, and SCGB1A1. Clusters 1 and 4 consist the peripheral zone, whereas other clusters are in the transition/central zone. **D,** Percentages of each cluster (clusters 1–6) in EPCAM$^+$ cells in HS196$^+$ and HS196$^-$ samples are shown. **E,** Expression of known prostate tumor markers by each cell/cluster is shown in the heatmap. Cells in the peripheral zone (clusters 1 and 4) are on the left side of the heatmap, and cells in the transition/central zone (clusters 2, 3, 5, and 6) are on the right side. AMACR expression is highlighted. **F,** HS196 positivity of AMACR$^+$ prostate cancer cells (total 81 cells among 984 EPCAM$^+$ cells) is shown. **G,** Serial frozen sections of the prostate specimen were used for H&E staining and RNA FISH. H&E pathology was coregistered with HS196 signal and an mRNA FISH image of AMACR. **H,** In the area of invasive prostate cancer, the presence of HS196-positive (magenta) and AMACR-expressing (green) prostate cancer cells was confirmed.

provide limited information about their potential biological behavior. Because biological behavior is frequently driven by aberrant signaling (4, 5), we hypothesized that detection of a global marker of this signaling could identify those tumors most likely to progress. Heat shock proteins, such as Hsp90, are critical chaperones involved in proper folding and trafficking of a number of molecules including oncogenic proteins (7–11). In prostate cancers, heat shock protein expression is associated with aggressive biology (38–40).

We previously demonstrated that an nIR-linked HSP90 targeting drug (HS131) could identify the most aggressive breast cancers (15). In order to develop a probe that could be imaged in deeper structures, we generated HS196, which consists of the same Hsp90 targeting drug linked to an nIR probe that fluoresces at a longer wavelength. We found that HS196 had a prolonged retention time within breast and prostate cancers in preclinical models, allowing imaging over an extended time period. In the human studies, HS196 was well tolerated with no significant toxicity and fluorescence could be detected in prostate cancers at both the cellular and tissue levels, demonstrating potential clinical utility for detecting in situ tumors and positive resection margins in real time during surgeries by using nIR imaging devices, such as Fluobeam.

An important advantage of imaging HSP90 with small-molecule drugs is that the probe is not perfusion dependent, but rather depends

on diffusion and specific binding, thus marking the cells with the highest Hsp90 expression. In our previous experience with HS131, we observed that surface expression of Hsp90 correlated with metastatic potential of breast cancer (15). Similarly, in prostate cancer, extracellular Hsp90 was shown to induce tumor growth, suppress E-cadherin, and initiate localized invasion dependent on EZH2 function (14) and was expressed by aggressive phenotypes (13). In the current studies, HS196 uptake was observed in multiple models of prostate cancer, including the most aggressively growing prostate subtypes. Detectable tissue levels by both direct quantitative measurement (LC/MS/MS) and fluorescence imaging of clinical specimens confirmed HS196 uptake by prostate cancers that were clinically diagnosed by preoperative MR imaging. Further, the single-cell sorting and confocal microscopy studies confirmed that in humans the HS196 also binds to and is retained by tumor cells, including neuroendocrine cells of the prostate, which have been linked to therapeutic resistance and progression (35, 41). This may also allow for earlier detection of neuroendocrine recurrence of prostate cancer, which is otherwise not identified by rising PSA. In fact, the PC-3 cell line, which demonstrated the greatest avidity for HS196 in our preclinical model, displays neuroendocrine differentiation (42).

In summary, as observed previously with HS131, the nIR dye-tethered Hsp90 inhibitor HS196, which has utility for imaging deeper

tumors and avoids the need for nuclear imaging, was able to detect multiple different subtypes of prostate cancer with the greatest uptake occurring in cancers with higher metastatic potential. Due to the rapid uptake and prolonged retention time of the HS196, it is feasible to administer it over a wide range of times before imaging, thus allowing for both conventional imaging and imaging during procedures such as surgery. Our next study is confirming the *in situ* fluorescence in humans undergoing biopsy of mammographically detected breast cancers.

In addition to imaging of prostate cancer with an Hsp90-targeted strategy, Hsp90 has also been studied as a therapeutic target in a variety of cancers, including prostate cancer. Although Hsp90 inhibitors as a monotherapy showed limited antitumor efficacy in clinical studies due to their toxicities, preliminary experience suggests that combination strategies with chemotherapeutic reagents or other small-molecule inhibitors may have more activity (12, 43–46). Furthermore, we have also developed a therapeutic version of our Hsp90-binding drug by replacing the near IR molecule with a photosensitizing molecule and demonstrating focal tumor destruction when laser light was applied (47). Studies of this molecule (HS201) are opening shortly.

Authors' Disclosures

Authors' Contributions

T. Osada: Formal analysis, validation, investigation, methodology, writing–original draft. **E.J. Crosby:** Formal analysis, investigation, methodology, writing–original draft. **K. Kaneko:** Formal analysis, investigation, writing–original draft. **J.C. Snyder:** Formal analysis, investigation, methodology, writing–original draft. **J.D. Ginzel:** Formal analysis, investigation, methodology, writing–original draft. **C.R. Acharya:** Formal analysis and investigation. **X.-Y. Yang:** Investigation and methodology. **T.J. Polascik:** Identify human subjects, provide patient care, and sample procurement. **I. Spasojevic:** Formal analysis, investigation, and methodology. **R.C. Nelson:** Formal analysis, writing–original draft. **A. Hobeika:** Project administration. **Z.C. Hartman:** Methodology, writing–original draft. **L.M. Neckers:** Writing–review and editing. **A. Rogatko:** Formal analysis, writing–original draft. **P.F. Hughes:** Resources, formal analysis, validation, investigation, writing–original draft. **J. Huang:** Formal analysis and investigation. **M.A. Morse:** Formal analysis, supervision, investigation, writing–original draft. **T. Haystead:** Resources, formal analysis, supervision, writing–original draft. **H.K. Lyerly:** Conceptualization, supervision, funding acquisition, and writing–original draft.

Acknowledgments

References

1. Epstein JI, Walsh PC, Carmichael M, Brendler CB. Pathologic and clinical findings to predict tumor extent of nonpalpable (stage T1c) prostate cancer. JAMA 1994;271:368–74.
2. Ploussard G, Epstein JI, Montironi R, Carroll PR, Wirth M, Grimm MO, et al. The contemporary concept of significant versus insignificant prostate cancer. Eur Urol 2011;60:291–303.
3. Matoso A, Epstein JI. Defining clinically significant prostate cancer on the basis of pathological findings. Histopathology 2019;74:135–45.
4. Hanahan D, Weinberg RA. Hallmarks of cancer: the next generation. Cell 2011; 144:646–74.
5. Srivastava S, Grizzle WE. Biomarkers and the genetics of early neoplastic lesions. Cancer Biomark 2010;9:41–64.
6. Fares J, Fares MY, Khachfe HH, Salhab HA, Fares Y. Molecular principles of metastasis: a hallmark of cancer revisited. Signal Transduct Target Ther 2020; 5:28.
7. Moulick K, Ahn JH, Zong H, Rodina A, Cerchietti L, Gomes DaGama EM, et al. Affinity-based proteomics reveal cancer-specific networks coordinated by Hsp90. Nat Chem Biol 2011;7:818–26.
8. Neckers L, Mollapour M, Tsutsumi S. The complex dance of the molecular chaperone Hsp90. Trends Biochem Sci 2009;34:223–6.
9. Vaughan CK, Neckers L, Piper PW. Understanding of the Hsp90 molecular chaperone reaches new heights. Nat Struct Mol Biol 2010; 17:1400–4.
10. Cheng Q, Chang JT, Geradts J, Neckers LM, Haystead T, Spector NL, et al. Amplification and high-level expression of heat shock protein 90 marks aggressive phenotypes of human epidermal growth factor receptor 2 negative breast cancer. Breast Cancer Res 2012;14:R62.
11. Whitesell L, Lindquist SL. HSP90 and the chaperoning of cancer. Nat Rev Cancer 2005;5:761–72.
12. Hoter A, Rizk S, Naim HY. The Multiple roles and therapeutic potential of molecular chaperones in prostate cancer. Cancers (Basel) 2019;11:1194.
13. Hance MW, Dole K, Gopal U, Bohonowych JE, Jezierska-Drutel A, Neumann CA, et al. Secreted Hsp90 is a novel regulator of the epithelial to mesenchymal transition (EMT) in prostate cancer. J Biol Chem 2012;287:37732–44.
14. Nolan KD, Franco OE, Hance MW, Hayward SW, Isaacs JS. Tumor-secreted Hsp90 subverts polycomb function to drive prostate tumor growth and invasion. J Biol Chem 2015;290:8271–82.
15. Osada T, Kaneko K, Gwin WR, Morse MA, Hobeika A, Pogue BW, et al. In vivo detection of HSP90 identifies breast cancers with aggressive behavior. Clin Cancer Res 2017;23:7531–42.
16. Eustace BK, Sakurai T, Stewart JK, Yimlamai D, Unger C, Zehetmeier C, et al. Functional proteomic screens reveal an essential extracellular role for hsp90 alpha in cancer cell invasiveness. Nat Cell Biol 2004;6:507–14.
17. McCready J, Sims JD, Chan D, Jay DG. Secretion of extracellular hsp90alpha via exosomes increases cancer cell motility: a role for plasminogen activation. BMC Cancer 2010;10:294.
18. Dunphy MPS, Pressl C, Pillarsetty N, Grkovski M, Modi S, Jhaveri K, et al. First-in-human trial of epichaperome-targeted PET in patients with cancer. Clin Cancer Res 2020;26:5178–87.
19. Crowe LB, Hughes PF, Alcorta DA, Osada T, Smith AP, Totzke J, et al. A fluorescent Hsp90 probe demonstrates the unique association between extracellular Hsp90 and malignancy in vivo. ACS Chem Biol 2017;12:1047–55.
20. Barrott JJ, Hughes PF, Osada T, Yang XY, Hartman ZC, Loiselle DR, et al. Optical and radioiodinated tethered Hsp90 inhibitors reveal selective internalization of ectopic Hsp90 in malignant breast tumor cells. Chem Biol 2013;20:1187–97.
21. Kozlowski JM, Fidler IJ, Campbell D, Xu ZL, Kaighn ME, Hart IR. Metastatic behavior of human tumor cell lines grown in the nude mouse. Cancer Res 1984; 44:3522–9.

22. Keer HN, Gaylis FD, Kozlowski JM, Kwaan HC, Bauer KD, Sinha AA, et al. Heterogeneity in plasminogen activator (PA) levels in human prostate cancer cell lines: increased PA activity correlates with biologically aggressive behavior. Prostate 1991;18:201–14.

23. Dozmorov MG, Hurst RE, Culkin DJ, Kropp BP, Frank MB, Osban J, et al. Unique patterns of molecular profiling between human prostate cancer LNCaP and PC-3 cells. Prostate 2009;69:1077–90.

24. Wu X, Gong S, Roy-Burman P, Lee P, Culig Z. Current mouse and cell models in prostate cancer research. Endocr Relat Cancer 2013;20:R155–70.

25. Becht E, McInnes L, Healy J, Dutertre CA, Kwok IWH, Ng LG, et al. Dimensionality reduction for visualizing single-cell data using UMAP. Nat Biotechnol 2019; 37:38–44.

26. Dehm SM, Schmidt LJ, Heemers HV, Vessella RL, Tindall DJ. Splicing of a novel androgen receptor exon generates a constitutively active androgen receptor that mediates prostate cancer therapy resistance. Cancer Res 2008; 68:5469–77.

27. Tepper CG, Boucher DL, Ryan PE, Ma AH, Xia L, Lee LF, et al. Characterization of a novel androgen receptor mutation in a relapsed CWR22 prostate cancer xenograft and cell line. Cancer Res 2002;62:6606–14.

28. Toutain PL, Bousquet-Mélou A. Plasma clearance. J Vet Pharmacol Ther 2004; 27:415–25.

29. Mitruka BM, Rawnsley HM. Clinical, biochemical and hematological reference values in normal experimental animals and normal humans. New York: Masson Publishing, 1981:413.

30. O'Connell KE, Mikkola AM, Stepanek AM, Vernet A, Hall CD, Sun CC, et al. Practical murine hematopathology: a comparative review and implications for research. Comp Med 2015;65:96–113.

31. Cameron JR, Skofronick JG, Grant RM. Physics of the body. 2nd ed. Madison, WI: Medical Physics Publishing, 1999:182.

32. Chernecky CC, Berger BJ, eds. laboratory tests and diagnostic procedures. 6th ed. St Louis, MO: Elsevier Saunders; 2013:620–1.

33. Henry GH, Malewska A, Joseph DB, Malladi VS, Lee J, Torrealba J, et al. A cellular anatomy of the normal adult human prostate and prostatic urethra. Cell Rep 2018;25:3530–42.

34. Beltran H, Rickman DS, Park K, Chae SS, Sboner A, MacDonald TY, et al. Molecular characterization of neuroendocrine prostate cancer and identification of new drug targets. Cancer Discov 2011;1:487–95.

35. Hu CD, Choo R, Huang J. Neuroendocrine differentiation in prostate cancer: a mechanism of radioresistance and treatment failure. Front Oncol 2015;5:90.

36. Leão R, Domingos C, Figueiredo A, Hamilton R, Tabori U, Castelo-Branco P. Cancer stem cells in prostate cancer: implications for targeted therapy. Urol Int 2017;99:125–36.

37. Mei W, Lin X, Kapoor A, Gu Y, Zhao K, Tang D. The contributions of prostate cancer stem cells in prostate cancer initiation and metastasis. Cancers (Basel) 2019;11:434.

38. Ciocca DR, Fanelli MA, Cuello-Carrion FD, Castro GN. Heat shock proteins in prostate cancer: from tumorigenesis to the clinic. Int J Hyperthermia 2010;26: 737–47.

39. Lisanti S, Garlick DS, Bryant KG, Tavecchio M, Mills GB, Lu Y, et al. Transgenic expression of the mitochondrial chaperone TNFR-associated protein 1 (TRAP1) accelerates prostate cancer development. J Biol Chem 2016;291:25247–54.

40. Ghosh S, Shinogle HE, Galeva NA, Dobrowsky RT, Blagg BS. Endoplasmic reticulum-resident heat shock protein 90 (HSP90) isoform glucose-regulated protein 94 (GRP94) regulates cell polarity and cancer cell migration by affecting intracellular transport. J Biol Chem 2016;291:8309–23.

41. Li Y, He Y, Butler W, Xu L, Chang Y, Lei K, et al. Targeting cellular heterogeneity with CXCR2 blockade for the treatment of therapy-resistant prostate cancer. Sci Transl Med 2019;11:eaax0428.

42. Tai S, Sun Y, Squires JM, Zhang H, Oh WK, Liang CZ, et al. PC3 is a cell line characteristic of prostatic small cell carcinoma. Prostate 2011;71:1668–79.

43. Oh WK, Galsky MD, Stadler WM, Srinivas S, Chu F, Bubley G, et al. Multicenter phase II trial of the heat shock protein 90 inhibitor, retaspimycin hydrochloride (IPI-504), in patients with castration-resistant prostate cancer. Urology 2011;78: 626–30.

44. Thakur MK, Heilbrun LK, Sheng S, Stein M, Liu G, Antonarakis ES, et al. A phase II trial of ganetespib, a heat shock protein 90 Hsp90) inhibitor, in patients with docetaxel-pretreated metastatic castrate-resistant prostate cancer (CRPC)—a prostate cancer clinical trials consortium (PCCTC) study. Invest New Drugs 2016;34:112–8.

45. Lamoureux F, Thomas C, Yin MJ, Fazli L, Zoubeidi A, Gleave ME. Suppression of heat shock protein 27 using OGX-427 induces endoplasmic reticulum stress and potentiates heat shock protein 90 inhibitors to delay castrate-resistant prostate cancer. Eur Urol 2014;66:145–55.

46. Ku S, Lasorsa E, Adelaiye R, Ramakrishnan S, Ellis L, Pili R. Inhibition of Hsp90 augments docetaxel therapy in castrate resistant prostate cancer. PLoS One 2014; 9:e103680.

47. Kaneko K, Osada T, Morse MA, Gwin WR, Ginzel JD, Snyder JC, et al. Heat shock protein 90-targeted photodynamic therapy enables treatment of subcutaneous and visceral tumors. Commun Biol 2020;3:226.

Molecular Cancer Therapeutics

HSP90-Specific nIR Probe Identifies Aggressive Prostate Cancers: Translation from Preclinical Models to a Human Phase I Study

Takuya Osada, Erika J. Crosby, Kensuke Kaneko, et al.

Updated version	Access the most recent version of this article at: doi:10.1158/1535-7163.MCT-21-0334
Supplementary Material	Access the most recent supplemental material at: http://mct.aacrjournals.org/content/suppl/2021/10/21/1535-7163.MCT-21-0334.DC1

Cited articles	This article cites 44 articles, 12 of which you can access for free at: http://mct.aacrjournals.org/content/21/1/217.full#ref-list-1

E-mail alerts	Sign up to receive free email-alerts related to this article or journal.
Reprints and Subscriptions	To order reprints of this article or to subscribe to the journal, contact the AACR Publications Department at pubs@aacr.org.
Permissions	To request permission to re-use all or part of this article, use this link http://mct.aacrjournals.org/content/21/1/217. Click on "Request Permissions" which will take you to the Copyright Clearance Center's (CCC) Rightslink site.